



Modelling, Calculation and Analysis of Electromagnetic Force and Vibroacoustic Behavior of Integer-Slot Permanent Magnet Synchronous Motor Considering Current Harmonics

Zhipeng Wu¹ · Shuguang Zuo¹ · Zhiyong Huang¹ · Xiaorui Hu¹ · Siyue Chen¹ · Chang Liu¹

Received: 21 October 2021 / Revised: 18 January 2022 / Accepted: 19 January 2022 / Published online: 19 February 2022
© Krishtel eMaging Solutions Private Limited 2022

Abstract

Background and Purpose The comfort of electric vehicles (EVs) is closely related to the vibroacoustic performance of integer-slot permanent magnet synchronous motors (ISPMSMs). This study provides a detailed investigation on the radial electromagnetic force and vibroacoustic behavior of ISPMSMs considering current harmonics.

Methods First, the origin and order feature of dead-time current harmonics are introduced and validated through the phase current test. Subsequently, a theoretical model of radial force considering dead-time current harmonics is built, the spatial and temporal characteristics of radial force are analyzed and verified via the 2-D Fourier decomposition. Then, a multiphysics model including the control model, the electromagnetic model, the equivalent structural model, and the acoustic radiation model is established to calculate the vibration and noise of an ISPMSM used for EVs. Moreover, the orthotropic material parameters of the stator and the non-uniform distribution of the radial force are also taken into account. The accuracy of the multiphysics model is validated through the vibration and noise tests. Finally, the vibroacoustic mechanism of the ISPMSM is clarified based on the multiphysics model, the effect of dead-time current harmonics on the vibration and noise is also analyzed.

Conclusions It is found that the 0-order and 2-order modal responses, which are commonly caused by the 0-order and slot-order radial forces, are the roots of vibration and noise in ISPMSMs. By changing the amplitudes of corresponding radial force harmonics, the dead-time current harmonics have a certain impact on the vibration and noise peaks, but the specific influence depends on their amplitudes and phase angles. This study provides guidance for the development of low-vibration and noise ISPMSMs.

Keywords Electric vehicle · Integer-slot permanent magnet synchronous motor · Radial electromagnetic force · Vibration · Noise · Dead-time current harmonics

Introduction

Electric vehicles (EVs) have become one of the best choices to mitigate the global energy crisis and environmental problems [1]. Due to high-power density, high efficiency, and high torque density, permanent magnet synchronous motors (PMSMs) have been widely used as driving motors in EVs

[2–4]. As a result, the vibration and noise issues of PMSMs, which are closely related to the comfort of EVs [5–7], have attracted extensive attention and become a research hotspot.

The vibration and noise of PMSMs can be classified into three categories: aerodynamic-, mechanical-, and electromagnetic vibration and noise [8]. Moreover, the electromagnetic vibration and noise induced by time-varying radial electromagnetic force acting on the stator teeth or permanent magnets are the dominant vibroacoustic source of low- and medium-rated PMSMs. At present, the calculation of electromagnetic vibration and noise contains analytical and numerical methods. In [9–11], the natural frequency and vibration response of the motors are analytically calculated based on the cylindrical shell vibration theory. Besides, in [12], an analytical model for vibration and noise prediction

✉ Shuguang Zuo
sgzuo@tongji.edu.cn

Zhipeng Wu
zpwu123@163.com

¹ School of Automotive Studies, Tongji University, Shanghai, China

in axial-flux motors is established based on the disc vibration theory. However, the analytical models in [9–12] are not accurate enough due to the modal characteristic variation caused by the stator structure simplification. Compared with analytical methods, numerical methods can calculate the electromagnetic vibration and noise more accurately by taking the real motor mechanical properties into account. In [13–15], the electromagnetic force acting on the stator teeth is equivalent to a concentrated force, and then applied to the structural finite-element (FE) model to calculate the vibration and noise of the motor. However, this loading method ignores the non-uniform distribution along the circumference of the electromagnetic force, which will induce extra errors in the vibration and noise simulations. To overcome the above problem, the nodal force mapping method (NFMM) is proposed in [16]. Besides the correct loading of electromagnetic force, an accurate structural FE model of the motor is also necessary for vibration and noise prediction. In [17–20], equivalent FE models of the stator and the winding are established by assigning orthotropic material parameters. However, due to small stiffness, the introduction of the winding in [17–20] will bring numerous local modes to the stator assembly, thereby increasing the calculation time and modal identification difficulty. Therefore, the equivalent modeling of the motor still needs further improvement.

It has been pointed out in previous studies that the vibration and noise of fractional-slot motors mainly come from the contribution of the lowest non-zeroth order radial force [9–12, 17, 18]. While for integer-slot motors, the vibration and noise mainly result from the 0-order modal response caused by the 0-order radial force [21–23]. However, the stator teeth modulation effect is neglected in the aforementioned studies. The high-order radial force can also arouse the low-order modal vibration via the modulation of stator teeth, thereby radiating acoustic noise. Specifically, the pole-order radial force of fractional-slot motors can be modulated [24]. Differently, the slot-order radial force of integer-slot motors can be modulated via the stator teeth, thereby arousing the 0-order modal vibration [25]. This indicates that the vibration and noise are actually comprehensive results of multi-order radial force. The discovery of the stator teeth modulation effect lays the foundation for the analysis of vibroacoustic behavior. To a better understanding, the vibroacoustic mechanism of integer-slot permanent magnet synchronous motors (ISPMSMs) including the dominant radial force and the dominant structural mode deserves further investigation by taking the modulation effect into consideration.

In addition, current harmonics are typical non-ideal factors, which have a significant influence on the vibroacoustic behavior of PMSMs. The PMSMs used for EVs generally adopt the space vector pulse width modulation (SVPWM). Affected by the SVPWM, there are abundant sideband

current harmonics around the carrier frequency [26, 27]. The effect of sideband current harmonics on sideband noise has been thoroughly studied in [28–30]. However, since the carrier frequency of PMSMs is quite high, the sideband noise is not sensitive to human ears. On the contrary, the dead-time current harmonics caused by the non-ideal electronic component characteristics of the inverter have a crucial effect on the low-frequency vibration and noise, thereby playing a significant role in the comfort of EVs. However, up to now, there are few studies on the influence of dead-time current harmonics on electromagnetic vibration and noise. Therefore, the specific influence of dead-time current harmonics on vibration and noise of ISPMSMs also deserves a thorough investigation.

The contribution of this study lies in that it provides a detailed analysis of the vibroacoustic behavior of ISPMSMs considering the dead-time current harmonics, which is beneficial for the electromagnetic force analysis, vibroacoustic prediction, and noise reduction. This paper is organized as follows. In Sect. 2, the origin and order feature of dead-time current harmonics are first analyzed and verified via the experimental test. Subsequently, the theoretical model of radial force is established considering dead-time current harmonics, and the spatial and temporal characteristics of radial force are determined and verified through the 2-D Fourier decomposition in Sect. 3. Then, a multiphysics model for vibration and noise calculation of the ISPMSM is established and validated through vibration and noise tests in Sect. 4. The vibroacoustic mechanism of the ISPMSM is also revealed. Finally, the specific influence of dead-time current harmonics on the maximum peaks of vibration and noise is detailed analyzed in Sect. 5.

Dead-Time Current Harmonic Analysis and Experimental Validation

Operation Principle of ISPMSM Used for EVs

As shown in Fig. 1, an ISPMSM with 8 poles and 24 slots used for micro-EVs is chosen in this paper. Its main

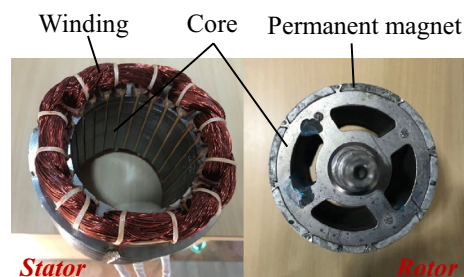


Fig. 1 Stator and rotor of the 8p24s ISPMSM

parameters are given in Table 1. Figure 2 shows the operation principle of the driving motor. First, the DC power supply will supply direct current to the controller according to the pedal signal. Then, combined with the rotor position signal generated by the motor position sensor, the inverter, which is integrated into the controller, will convert the direct current to a three-phase alternating current through a certain modulation strategy to maintain the motor operation and torque output. Finally, the operation of the driving motor achieves a closed-loop through the time-varying pedal signal and the real-time feedback rotor position signal.

However, due to non-ideal control factors, the current modulation will produce lots of harmonic components in the three-phase current, which will influence the radial force and vibroacoustic behavior of the driving motor, and further deteriorate the NVH performance of EVs.

Analysis and Validation of Dead-Time Current Harmonics

The low-order current harmonics caused by the characteristics of inverter switching electronic components, namely the dead-time current harmonics, have an important influence on the low-frequency vibration and noise of the driving motor. Hence, this study focuses on the effect of dead-time current harmonics on radial force and vibroacoustic behavior of the ISPM SM.

The mechanism for the generation of dead-time current harmonics is introduced in this section. As shown in Fig. 3a, the trigger signals of the upper and lower bridge arms of the inverter switch are complementary under ideal conditions. However, the opening and closing operation of the upper and the lower bridge arms actually need a certain time. Generally, the open time is less than the close time, so it is easy to induce the short-circuit fault that both the upper and the lower bridge arms are conducted simultaneously. To avoid the above short-circuit fault, the method that the closing operation is ahead of the opening operation is usually

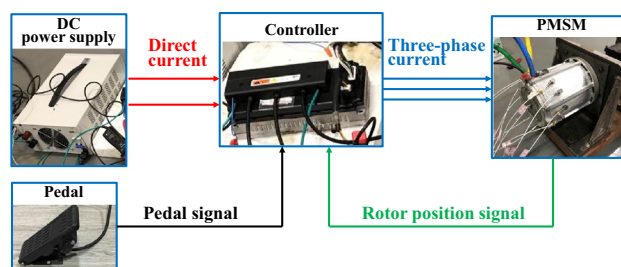


Fig. 2 Operation principle of the ISPM SM used for micro-EVs

adopted, which will lead to a delay between the two trigger signals, namely, the dead time, as shown in Fig. 3a.

As shown in Fig. 3b, the dead time will induce errors in the three-phase voltage, namely the dead-time voltage error, whose amplitude depends on the DC bus voltage U_{dc} and the dead-time T_d . The three-phase dead-time voltage error can be expressed as

$$\begin{bmatrix} u_{ae} \\ u_{be} \\ u_{ce} \end{bmatrix} = \frac{4T_d f_s}{\pi} U_{dc} \begin{bmatrix} \sum_k \frac{1}{2k-1} \sin[(2k-1)p\omega t] \\ \sum_k \frac{1}{2k-1} \sin[(2k-1)(p\omega t - \frac{2}{3}\pi)] \\ \sum_k \frac{1}{2k-1} \sin[(2k-1)(p\omega t + \frac{2}{3}\pi)] \end{bmatrix} \tag{1}$$

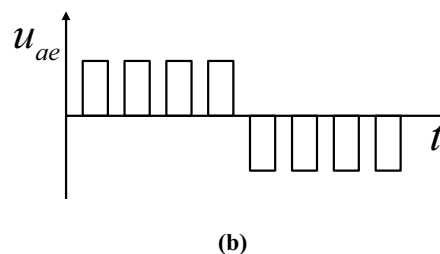
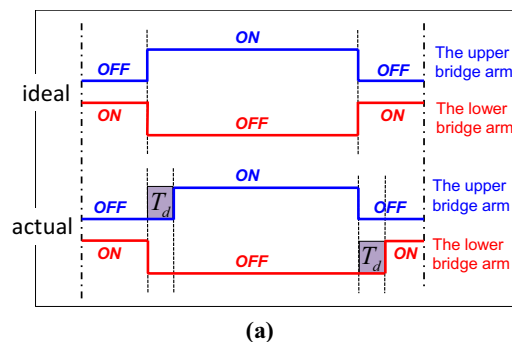


Fig. 3 Dead time and dead-time voltage of the inverter a dead time; b dead-time voltage

Table 1 Main parameters of the 8p24s ISPM SM

Parameter	Symbol	Value
Pole/slot number	$2p/Q$	8/24
Inner radius of stator	R	44 mm
Air-gap length	g	1 mm
PM thickness	h_{PM}	4 mm
Axial length of stator	L	84 mm
PM remanence	B_r	1.25 T
Pole-arc coefficient	α_p	0.84
Maximum power	P_{max}	10 kW
Maximum speed	V_{max}	3200 rpm

here, u_{ae}, u_{be} and u_{ce} represent the three-phase dead-time voltage error, f_s is the switching frequency, p is the pole-pair number, ω is the mechanical angular velocity. It can be seen from (1) that the frequency of dead-time voltage harmonics is odd times of the current fundamental frequency. For star-connected windings, the harmonics with orders of three and its multiples will cancel each other out. Therefore, the three-phase current considering $(6k \pm 1)$ th dead-time current harmonics can be written as

$$\begin{bmatrix} i_a \\ i_b \\ i_c \end{bmatrix} = \begin{bmatrix} i_1 \sin(p\omega t + \varphi_1) + \sum_k i_{6k\pm 1} \sin[(6k \pm 1)p\omega t + \varphi_{6k\pm 1}] \\ i_1 \sin(p\omega t - \frac{2}{3}\pi + \varphi_1) + \sum_k i_{6k\pm 1} \sin[(6k \pm 1)(p\omega t - \frac{2}{3}\pi) + \varphi_{6k\pm 1}] \\ i_1 \sin(p\omega t + \frac{2}{3}\pi + \varphi_1) + \sum_k i_{6k\pm 1} \sin[(6k \pm 1)(p\omega t + \frac{2}{3}\pi) + \varphi_{6k\pm 1}] \end{bmatrix} \quad (2)$$

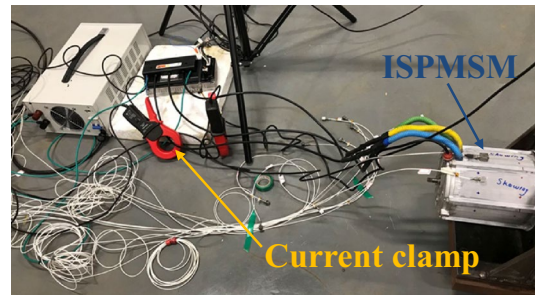
here, i_a, i_b and i_c represent the three-phase current, i_1 and φ_1 are the amplitude and phase angle of the fundamental current, respectively, $i_{6k\pm 1}$ and $\varphi_{6k\pm 1}$ are the amplitude and phase angle of the $(6k \pm 1)$ th current harmonics, respectively. Due to the low-order properties (frequency properties), the dead-time current harmonics will have a significant impact on the radial force and vibroacoustic behavior of the driving motor.

To validate the above theoretical analysis, the phase current of the 8p24s ISPMSM at 3200 r/min is tested through the current clamp, as shown in Fig. 4a. Then, the current harmonics are obtained via the fast Fourier decomposition. Figure 4b shows the main harmonics of the phase current. Since the motor runs at the speed of 3200 r/min, so the current fundamental frequency f_e is 213.33 Hz ($f_e = \frac{np}{60} = \frac{3200 \times 4}{60} = 213.33 \text{ Hz}$). It can be seen from Fig. 4b that the orders of the main current harmonics are 5th, 7th, 11th and etc., satisfying $(6k \pm 1)$ th, which is consistent with the above theoretical analysis.

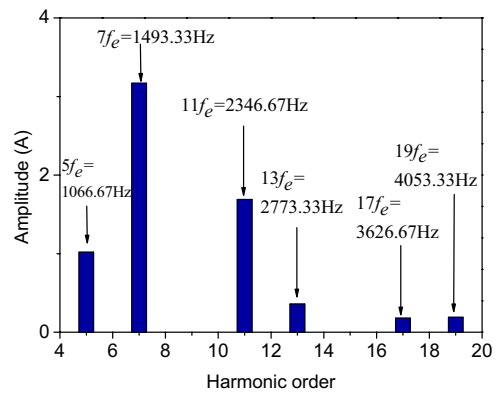
Modelling, Analysis and Validation of Radial Electromagnetic Force Considering Current Harmonics

Theoretical Modelling and Analysis of Radial Force Considering Dead-Time Current Harmonics

The electromagnetic vibration and noise of ISPMSMs mainly come from the radial force acting on the teeth surfaces, and the vibroacoustic behavior is closely related to the spatial and temporal characteristics of radial force harmonics. Therefore, it is necessary to establish a theoretical model considering dead-time current harmonics and analyze the spatiotemporal distribution characteristics of radial force harmonics.



(a)



(b)

Fig. 4 Phase current harmonics at 3200 r/min tested by the current clamp **a** test environment; **b** current harmonics

For slotless ISPMSMs, the PM field B_{r_mag} and the armature reaction field B_{r_arm} in the air-gap can be expressed in terms of the following Fourier series.

$$B_{r_mag} = \sum_n B_{mn} \cos[np(\theta - \omega t)] \quad (3)$$

$$B_{r_arm} = \sum_h \sum_v B_{av}^h \sin(vN_t \theta - s_{vh} h p \omega t + \theta_h) \quad (4)$$

here, B_{mn} is the amplitude of the np th PM field harmonic, n is an odd number, B_{av}^h is the vN_t th armature reaction field harmonic generated by the h th current harmonic. N_t is the spatial period number of motor, θ_h is the phase angle of h th current harmonic, $s_{vh} = \pm 1$, and its sign depends on the rotation direction of armature reaction field and phase sequence of current harmonics.

The stator slotting effect of ISPMSMs can be calculated by the following relative permeance function.

$$\lambda_a = \lambda_0 + \sum_u \lambda_{au} \cos(uQ\theta) \quad (5)$$

here, λ_a is the relative permeance, λ_0 is the DC component, λ_{au} is the amplitude of u th relative permeance harmonic, Q is the slot number.

Furthermore, the total air-gap field B_r considering the dead-time current harmonic and the stator slotting effect can be given as

$$B_r = (B_{r_mag} + B_{r_arm})\lambda_a \tag{6}$$

According to the Maxwell stress tensor method, the radial force can be written as

$$f_r \approx \frac{B_r^2}{2\mu_0} \tag{7}$$

here, μ_0 is the vacuum permeability. By substituting (3)–(6) into (7), the specific expression of radial force can be obtained through trigonometric function simplification. Note that some radial force harmonics, such as harmonics generated by the interaction of permanence harmonics and armature reaction field harmonics, can be ignored due to their tiny amplitudes. Hence, the expression of radial force, which only considers the main force harmonics, can be given as

$$\begin{aligned} f_r \approx & \frac{1}{4\mu_0} \lambda_0^2 \sum_{n_1} \sum_{n_2} B_{mn_1} B_{mn_2} \left\{ \begin{aligned} & \cos[(n_1 + n_2)p\theta - (n_1 + n_2)p\omega t] \\ & + \cos[(n_1 - n_2)p\theta - (n_1 - n_2)p\omega t] \end{aligned} \right\} \\ & + \frac{1}{4\mu_0} \lambda_0 \sum_{n_1} \sum_{n_2} \sum_u B_{mn_1} B_{mn_2} \lambda_{au} \left\{ \begin{aligned} & \cos\{[(n_1 + n_2)p \pm uQ]\theta - (n_1 + n_2)p\omega t\} \\ & + \cos\{[(n_1 - n_2)p \pm uQ]\theta - (n_1 - n_2)p\omega t\} \end{aligned} \right\} \\ & + \frac{1}{2\mu_0} \lambda_0^2 \sum_n \sum_h \sum_v B_{mn} B_{av}^h \left\{ \begin{aligned} & \sin[(np + vN_t)\theta - (n + s_{vh}h)p\omega t + \theta_h] \\ & + \sin[(np - vN_t)\theta - (n - s_{vh}h)p\omega t + \theta_h] \end{aligned} \right\} \\ & + \frac{1}{2\mu_0} \lambda_0 \sum_n \sum_h \sum_v \sum_u B_{mn} B_{av}^h \lambda_{au} \left\{ \begin{aligned} & \sin\{[(np + vN_t) \pm uQ]\theta - (n + s_{vh}h)p\omega t + \theta_h\} \\ & + \sin\{[(np - vN_t) \pm uQ]\theta - (n - s_{vh}h)p\omega t - \theta_h\} \end{aligned} \right\} \end{aligned} \tag{8}$$

Sources, spatial orders and frequencies of radial force harmonics can be directly determined according to (8). The specifications are summarized in Table 2. Since n is an odd number, it can be deduced from Table 2 that the spatial order of radial force of ISPMsMs includes 0 and 2 kp. Moreover, the frequency of radial force satisfies 2 kpf as a whole, namely the pole frequency. Furthermore, the frequency characteristics of radial force of any spatial order can also be derived according to Table 2. For example, it can be analytically derived that the frequencies of both the 0-order and 24-order radial forces satisfy 6 kpf.

The introduction of dead-time current harmonics will not change the spatial and temporal characteristics of radial force harmonics, but will have a significant influence on their amplitudes. These laws about radial force lay the foundation for vibration and noise analysis of ISPMsMs.

Validation Through Electromagnetic FE Analysis

The theoretical analysis of radial force is verified through the FE method in this section. First, as shown in Fig. 5, a 2-D electromagnetic model of the 8p24s ISPMsM is established in the JMAG software. The accuracy of the electromagnetic model is validated through the back electromotive force (BEMF) test. Figure 6 shows the comparison results of BEMFs under 1000 r/min. It can be seen that the simulated result agrees well with the tested result, validating the accuracy of the established electromagnetic model.

Then, as shown in Fig. 7, the field-oriented vector control model of the ISPMsM is established in Simulink. Dur-

ing simulation analysis, the dead time is set to be 5 μ s,

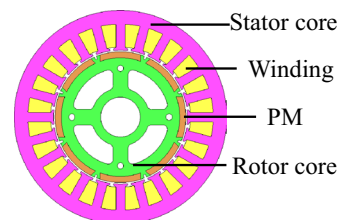


Fig. 5 A 2-D electromagnetic model of the 8p24s ISPMsM

Table 2 Source and spatiotemporal characteristics of radial force in ISPMsMs

Source	Spatial order	Frequency
PM field	$(n_1 \pm n_2)p$	$(n_1 \pm n_2)pf$
Interaction of PM field and stator slot	$(n_1 \pm n_2)p \pm uQ$	$(n_1 \pm n_2)pf$
Interaction of PM field and armature reaction field	$np \pm vN_t$	$(n \pm s_{vh}h)pf$
Interaction of PM field, stator slot and armature reaction field	$(np \pm vN_t) \pm uQ$	$(n \pm s_{vh}h)pf$

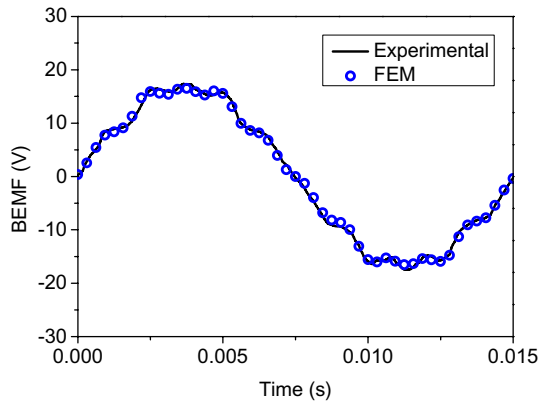


Fig. 6 Comparison of BEMF of the ISPMSM under 1000 r/min

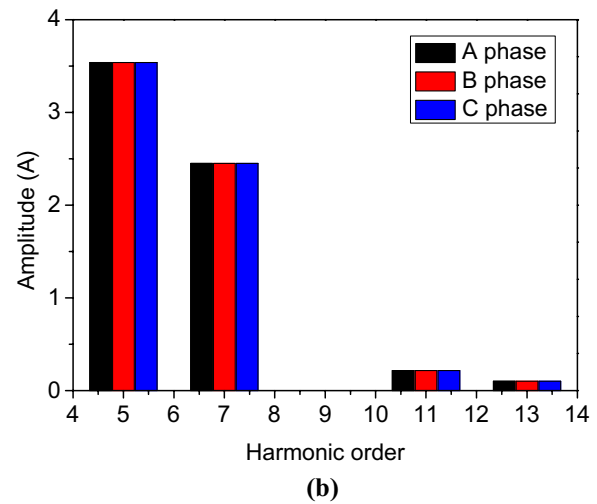
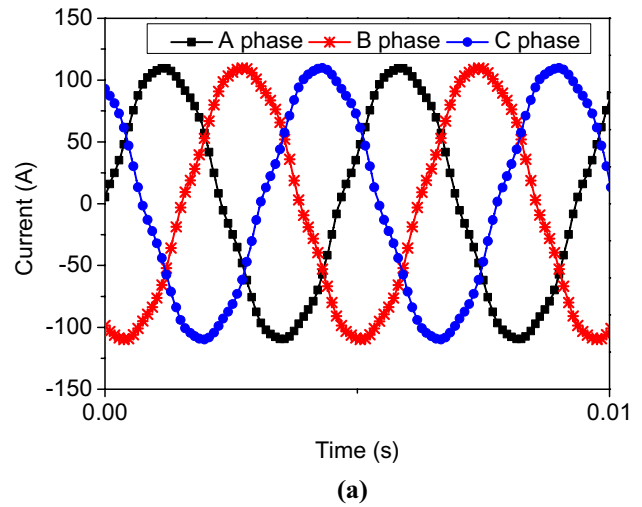


Fig. 8 Three-phase current considering the dead time a waveform; b dead-time current harmonics

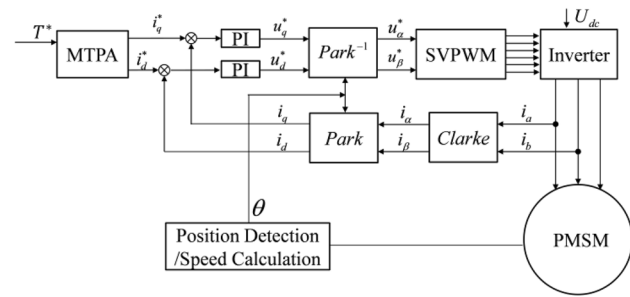


Fig. 7 Field-oriented vector control model of the ISPMSM

and the output three-phase current of the control model, which contains dead-time current harmonics, serves as the input of the electromagnetic force calculation. Figure 8a, b shows the waveform and main harmonics of the output three-phase current at 3200 r/min, respectively. It can be seen that when considering the dead time, the three-phase current is no longer sinusoidal, but contains the 5th, 7th, 11th, and 13th harmonic components, which is consistent with the theoretical analysis in Sect. 2.2.

Figure 9a shows the waveform of the radial force under dead-time current supply. It can be seen that the radial force acting on the stator teeth changes simultaneously in the time and space domain. As shown in Fig. 9b, the spatial and temporal distribution characteristics of the radial force are obtained through the 2-D Fourier decomposition. It can be found that the introduction of dead-time current harmonics does not change the spatiotemporal properties of the radial force. Specifically, the spatial order still contains 0 and 2 kp, while the frequency still satisfies 2 kpf. This is consistent with the conclusions in Table 2. However, as the source of the radial force is more abundant with the introduction of dead-time current harmonics, the

amplitude of radial force has changed, which will generate a certain influence on the vibration and noise peaks.

Multiphysics Model for Vibration and Noise Prediction and Experimental Validation

Stator Structural Model Considering Orthotropic Material Parameters

The components of the ISPMSM mainly include stator core, winding, enclosure and end covers. As the stator core is stacked with silicon steel sheets along the axial direction and the winding is stacked with copper wires, the stator core and winding exhibit different mechanical properties in different directions. To establish an accurate equivalent structural model, it is necessary to identify the orthotropic material

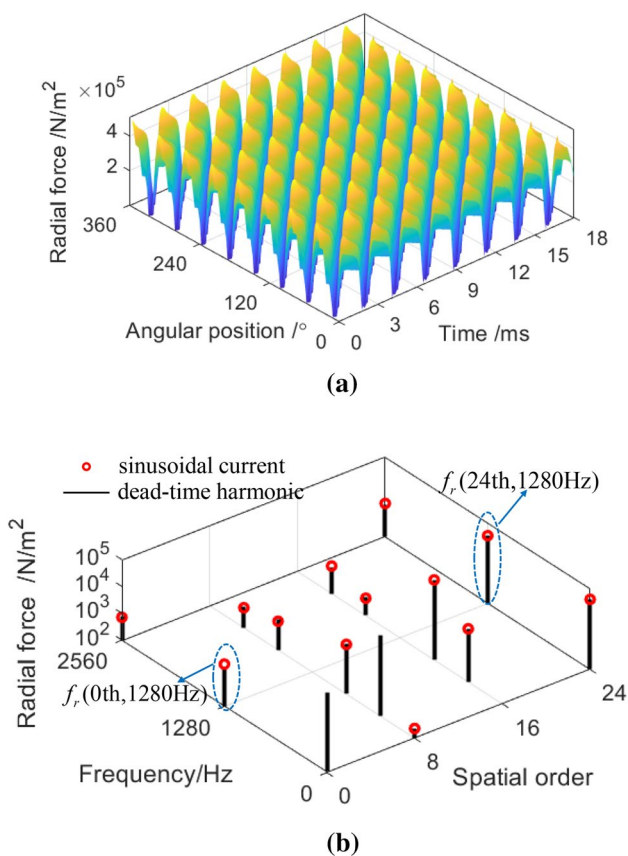


Fig. 9 Spatial and temporal distribution of radial force at 3200 r/min **a** waveform; **b** harmonic components

parameters of the stator, which mainly include the elastic modulus and shear modulus. In this section, the orthotropic material parameters of the stator are identified through modal tests. Figure 10 shows the modal test environments of the stator core, stator, and whole motor. During modal tests, the excitation force is generated by the force hammer, while the vibration response is captured by acceleration sensors. The tested modal characteristics including modal shapes and modal frequencies are recorded in Table 3.

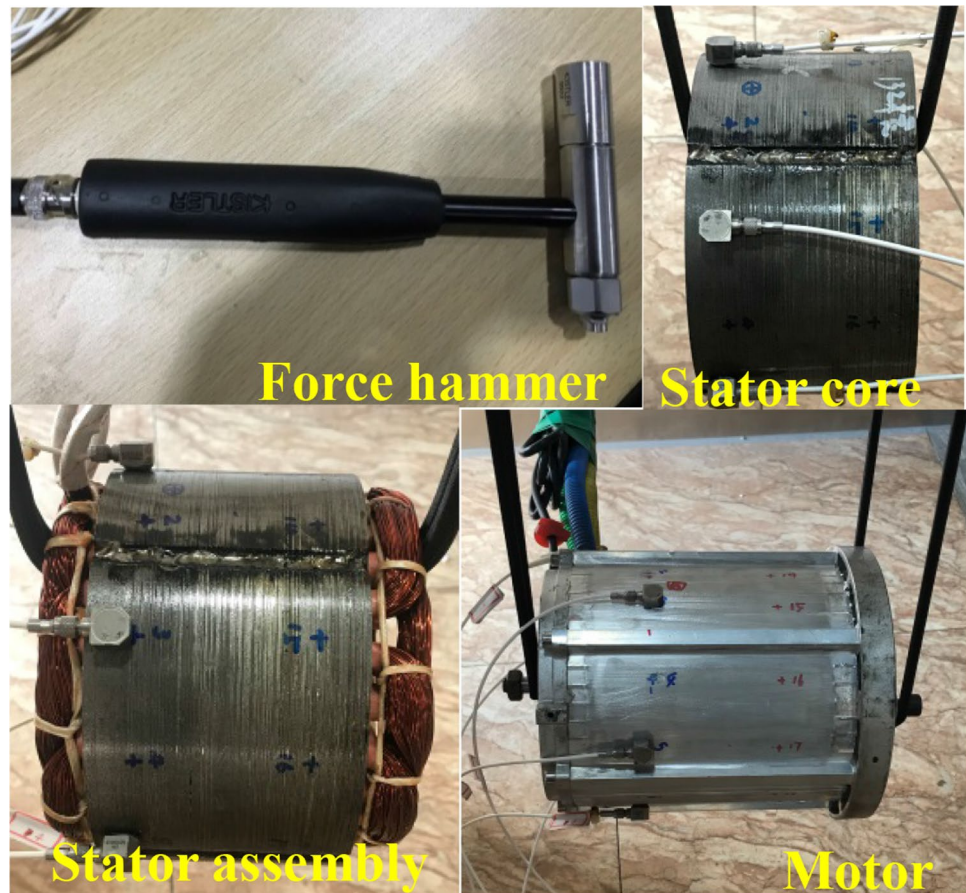
The detailed identification process of orthotropic material parameters is listed as follows. As shown in Fig. 11, an equivalent structural model of the stator core is first established in ANSYS software. Then, making the simulated modal frequencies of the stator core move close to the tested results by adjusting material parameters (E_x , E_y , E_z , G_{xy} , G_{yz} , G_{zx}) of the FE model. Note that, due to the tiny influence of the Poisson’s ratio on modal characteristics, an empirical value of 0.3 is adopted in the modal simulation analysis. Finally, the comparison of modal shapes and modal frequencies of the stator core is recorded in Table 3. It can be found that tiny relative errors between the simulated and tested frequencies are achieved by assigning orthotropic material parameters. This means

that the real modal characteristics of the stator core can be well revealed by the equivalent structural model.

The geometry of the winding is irregular, which makes its mass distribution and stiffness distribution extremely complicated. As a result, it is difficult to establish an accurate structural model of the winding. Besides, since the stiffness is quite small, the introduction of the winding will bring lots of local modes to the stator, thereby adding the calculation time and modal identification difficulty. In fact, the effect of the winding on the stator can be attributed to the mass effect and the stiffness effect. To reduce local modes and simplify the modal identification process, the additional mass method is adopted in this paper. The real mass of the winding is added to the 48 teeth surfaces (red surfaces in Fig. 11). Subsequently, making the simulated modal frequencies move close to the tested results by adjusting the equivalent material parameters of the stator. In this process, the stiffness effect of the winding has been equivalent to the material parameters of the stator core. The comparison of modal frequencies of the stator is also summarized in Table 3 (since the modal shapes of the stator are similar to that of the stator core, they are neglected in Table 3). It can be seen that the simulated modal frequencies of the stator agree well with the tested results. It should point out that since the real mass of the winding is only added to the teeth surfaces, and the end effect of the winding is ignored, there are still some errors between the simulated and tested results. But they are acceptable for vibration and noise calculation. Finally, the identified orthotropic material parameters are listed in Table 4. Note that E_w (200 GPa) and G_w (80 GPa) are elastic modulus and shear modulus of steel, respectively.

To further verify the accuracy of the identified orthotropic material parameters in Table 4, the modal simulation analysis of the whole motor is further implemented. As the enclosure and end covers are continuous elastomers, only real material parameters need to be assigned to their structural models. The modal simulation results of the whole motor are also compared with the experimental results, as shown in Table 3. It can be seen that the average relative error of symmetrical modes of the whole motor, which contribute most to straight-slot motors, is only 1.97%. This illustrates that the established equivalent structural model of the ISPM SM is accurate enough for vibration and noise calculation. It should be pointed out that to simulate the constraint conditions in the vibration and noise tests, shown in Fig. 16, a fixed support constraint is imposed on the surface of the rear end cover of the whole motor, as shown in Fig. 12. The corresponding constraint modal frequencies are also recorded in Table 3. Moreover, the constraint modal characteristics of the whole motor will be further used in the numerical calculation of vibration and noise.

Fig. 10 Modal tests of stator core, stator, and whole motor



Multiphysics Model for Electromagnetic Vibration and Noise Prediction

On the basis of current harmonics, radial force and structural modal analysis, a multiphysics model for electromagnetic vibration and noise prediction is established in this section. The multiphysics model integrates the control model, the electromagnetic model, the equivalent structural model, and the acoustic radiation model. The specific calculation process of electromagnetic vibration and noise is shown in Fig. 13.

First, the operation condition of the ISPMMSM including the target torque and rotation speed is simulated by the control model. The three-phase current considering dead-time current harmonics, which will be used as the input of electromagnetic simulation, can be obtained by setting the dead time. Subsequently, the electromagnetic force can be calculated by the 2-D electromagnetic model. It is assumed that the electromagnetic force of straight-slot motors is evenly distributed along the axial direction, so the 2-D electromagnetic force can be expanded to the 3-D electromagnetic force. Then the 3-D electromagnetic force is transferred from the electromagnetic mesh to the structural mesh via the NFMM. Since the non-uniform distribution characteristic of electromagnetic force is

unchanged, the NFMM is more accurate than the concentrated force loading method. The NFMM can be expressed as

$$\sigma_{mesh,k} = \frac{\sum_i^{N_{mag}} \sigma_{mesh,i} \cdot A_{mag,i}}{A_{mesh,k}} \quad (9)$$

here, $\sigma_{mesh,k}$ and $\sigma_{mesh,i}$ are the force densities in the structural mesh and electromagnetic mesh with the corresponding areas $A_{mesh,k}$ and $A_{mag,i}$. N_{mag} is the number of mesh elements whose centroid is positioned within the area of the mechanical element $A_{mesh,k}$. After the nodal force mapping, the electromagnetic force acting on the structural mesh is shown in Fig. 14.

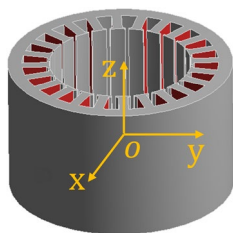
Based on the nodal force acting on the structural mesh and the constraint modal characteristics of the equivalent structural model, the electromagnetic vibration of the ISPMMSM is calculated through the MSM. The calculation equations of MSM can be given as

$$[M] \sum_{i=1}^N \{\Phi_i\} \ddot{x}_i + [C] \sum_{i=1}^N \{\Phi_i\} \dot{x}_i + [K] \sum_{i=1}^N \{\Phi_i\} x_i = \{F\} \quad (10)$$

Table 3 Comparison of modal characteristics of stator core, stator and whole motor

Modal shape and modal frequency	Mode number					
	(0, 2)	(1, 2)	(0, 3)	(1, 3)	(0, 4)	(1, 4)
Stator core						
Tested modal shape						
Simulated modal shape						
Tested modal frequency	998 Hz	1240 Hz	2580 Hz	2970 Hz	4650 Hz	5020 Hz
Simulated modal frequency	991 Hz	1245 Hz	2623 Hz	3013 Hz	4622 Hz	4983 Hz
Relative error	0.7%	0.4%	1.67%	1.45%	0.6%	0.74%
Stator						
Tested modal frequency	919 Hz	1130 Hz	2340 Hz	2660 Hz	4570 Hz	5220 Hz
Simulated modal frequency	916 Hz	1118 Hz	2432 Hz	2708 Hz	4207 Hz	4423 Hz
Relative error	0.3%	1.1%	3.9%	1.8%	7.9%	15.3%
Whole motor						
Tested modal shape						
Simulated modal shape						
Tested modal frequency	1210 Hz	2260 Hz	3000 Hz	3890 Hz	4780 Hz	5770 Hz
Simulated modal frequency	1205 Hz	2388 Hz	2842 Hz	3786 Hz	4772 Hz	5360 Hz
Relative error	0.4%	5.7%	5.3%	2.7%	0.2%	7.1%
Constrained modal frequency	1270 Hz	2420 Hz	2855 Hz	3811 Hz	4777 Hz	5365 Hz

Fig. 11 Equivalent structural model of the stator



here, x_i is the nodal displacement in modal coordinates, $\{\Phi_i\}$ is the modal shape of mode i , $\{F\}$ is the electromagnetic nodal force, N is the number of modes to be summed, $[M]$, $[C]$ and $[K]$ are the mass matrix, the damping matrix and the stiffness matrix, respectively.

Finally, as shown in Fig. 15, an acoustic model of the ISPMSM, which includes the enclosed acoustic mesh and field point mesh, is established. To keep consistent with the test conditions, the radius of the field point mesh is set as 0.5 m. The vibration acceleration calculated by the MSM is used as the acoustic boundary condition, and the electromagnetic noise is calculated by the BEM.

To validate the accuracy of the established multiphysics model, the vibration and noise tests of the ISPMSM are performed in a semi-anechoic room. Figure 16 shows the experimental environment. In the tests, the ISPMSM is rigidly mounted on the bench by bolts. The motor is operated stably at a maximum speed of 3200 r/min by adjusting the pedal. The corresponding vibration and noise signals are captured by acceleration sensors and microphones,

Table 4 Orthotropic material parameters of stator

Material parameters	Young's modulus	Shear modulus	Poisson's ratio	Density (kg/m ³)
Stator core	$E_x = E_y = 104.8\%E_w$ $E_z = 100\%E_w$	$G_{xy} = 131.25\%G_w$ $G_{yz} = G_{zx} = 25\%G_w$	0.3	7305

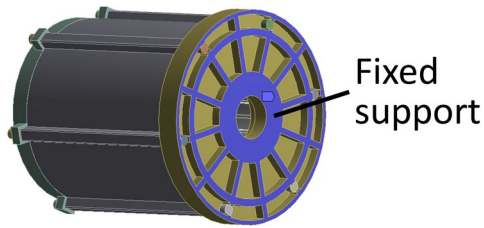


Fig. 12 Constraint condition of the whole motor

then collected and processed by the data collection system. The vibration and noise under the same operation conditions are also simulated using the multiphysics model. Figure 17 exhibits the comparison results of vibration and noise. It can be seen that the simulated results agree well with the tested results. This illustrates that the established multiphysics model is accurate enough for reflecting the main peaks and the overall variation trend of vibration and noise of the ISPMSM. However, it should emphasize that some noise errors still exist at some frequencies. These errors mainly come from two aspects, one is the variation of modal characteristics, and the other is the mechanical noise. Although the orthotropic material parameters are adopted during the equivalent modeling, some errors still exist between the simulated and tested modal frequencies. Moreover, an empirical value of the damping ratio is assigned to each mode in the multiphysics model, which may also bring extra noise errors. In addition, the tested noise not only contains the electromagnetic noise but also the mechanical noise generated by the bearings.

As shown in Fig. 17, both the maximum peaks of vibration and noise occur at 1280 Hz. To analyze the vibroacoustic mechanism of the ISPMSM, the modal participation factor (MPF) at 1280 Hz is extracted from the LMS Virtual.Lab software, as shown in Fig. 18. It can be observed that the electromagnetic vibration and noise of straight-slot motors

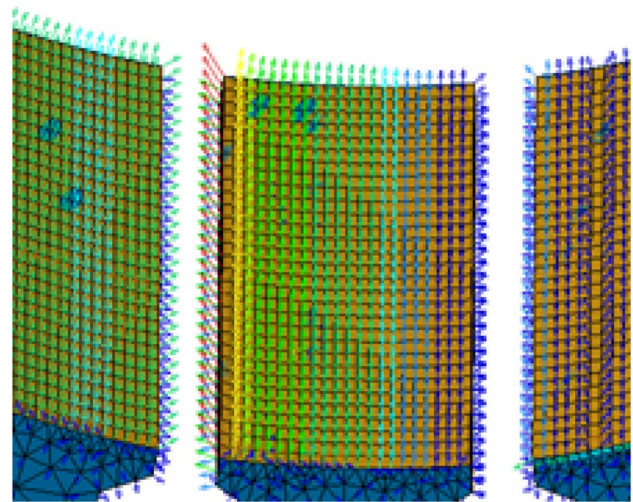


Fig. 14 Nodal force on structural mesh

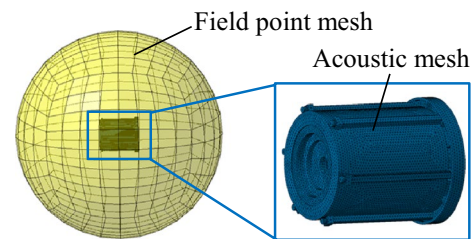


Fig. 15 Acoustic model of the whole motor

mainly come from the contribution of symmetrical modes. Moreover, in addition to the zeroth mode, the second mode is also crucial to the vibroacoustic behavior of the ISPMSM. This is different from the conclusion in previous literature, which believes that only the zeroth mode (breathing mode) is the dominant mode of vibration and noise of ISPMSMs.

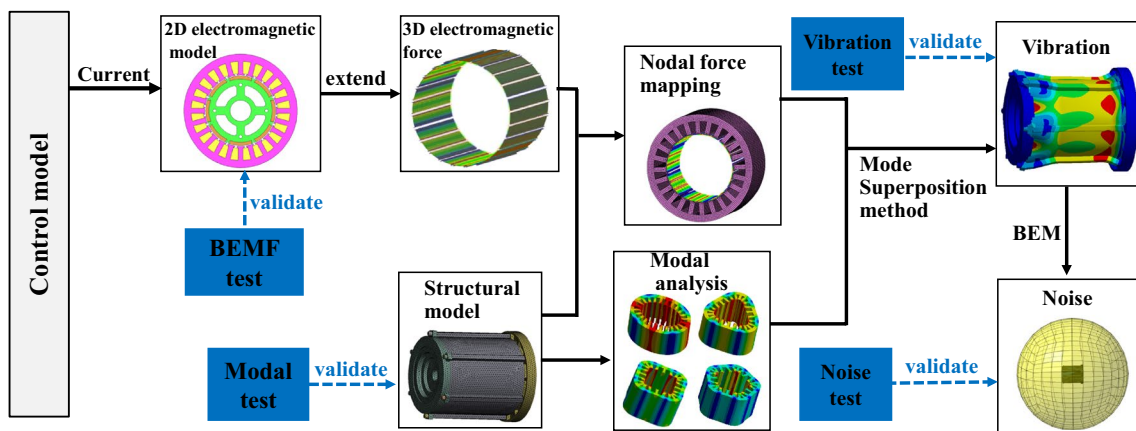


Fig. 13 Calculation process of electromagnetic vibration and noise

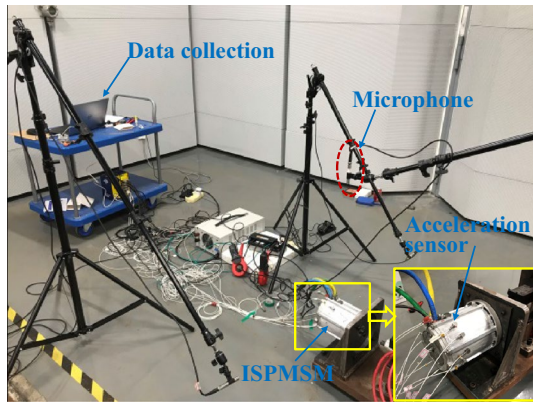


Fig. 16 Vibration and noise test of the ISPMSM

Fig. 17 Comparison of simulated and tested results at 3200 r/min **a** vibration; **b** noise

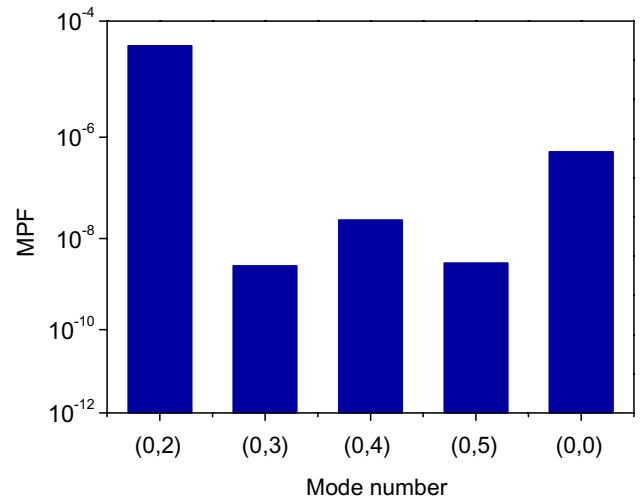
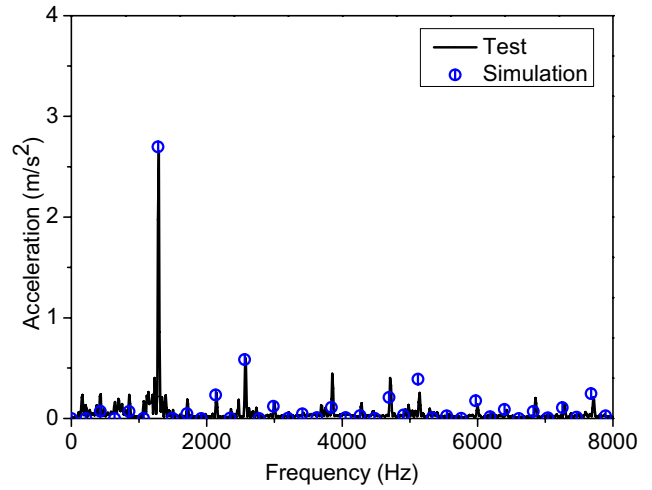
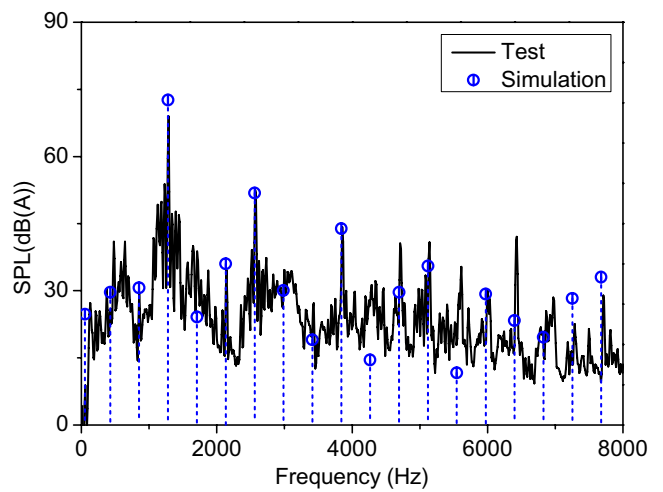


Fig. 18 Modal participation factor at 1280 Hz



(a)



(b)

In fact, the ISPMSMs used for EVs usually have a high 0-order modal frequency. Therefore, the 0-order modal vibration is actually a forced vibration that the structural mode satisfies the spatial match with the corresponding radial force. In addition, at 1280 Hz, the frequency of the corresponding radial force is very close to the 2-order constraint modal frequency (1270 Hz). Therefore, the 2-order modal vibration is actually a resonance satisfying frequency match. Considering the modulation effect of the slotted stator structure, the maximum peaks of vibration and noise at 1280 Hz mainly come from the 1280-Hz 0-order and 24-order radial force harmonics. And the specific influence depends on their amplitudes. This illustrates that the vibroacoustic behavior of ISPMSMs is actually a comprehensive result of radial force harmonics with different spatial orders, not only attributes to the 0-order force. Therefore, the vibroacoustic mechanism of ISPMSMs in the traditional analysis is further improved in this study through the analysis of dominant structural mode and dominant radial force. Furthermore, using the established multiphysics model, the effect of dead-time current harmonics on vibroacoustic behavior of the ISPMSM will be analyzed in detail in Sect. 5.

Effect of Dead-Time Current Harmonics on Vibroacoustic Behavior of ISPMSM

To analyze the influence of dead-time current harmonics, the vibration and noise at 3200 r/min both under sinusoidal and dead-time currents are calculated using the established multiphysics model. During the simulation, the amplitude and phase sequence of dead-time current harmonics are summarized in Table 5, and the amplitude of the sinusoidal current is equal to that of the fundamental wave of dead-time current. Specific simulation results are exhibited in Fig. 19. It can be seen that the vibration and noise peaks appear at the frequency of 2 kpf under both two load conditions. This indicates that the dead-time current harmonics do not produce extra vibration and noise orders. However, the dead-time current harmonics have a certain impact on the vibration and noise peaks due to the variation of electromagnetic

Table 5 Amplitude and phase sequence of fundamental and harmonic current

Order	Amplitude (A)	Phase sequence
1	110.22	ABC
5	3.5365	ACB
7	2.4486	ABC
11	0.2156	ACB
13	0.1012	ABC

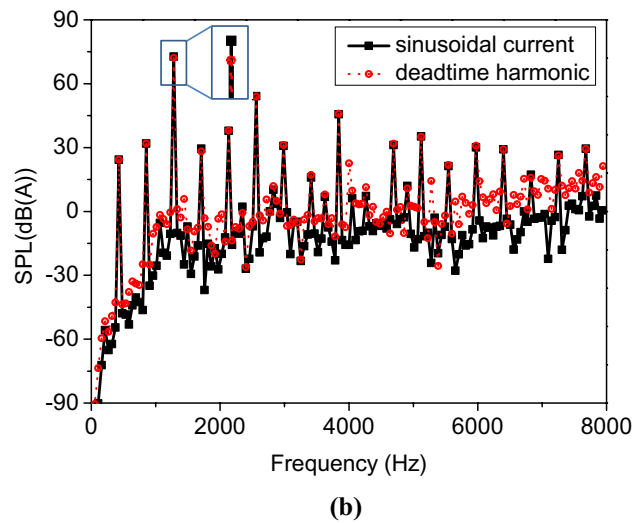
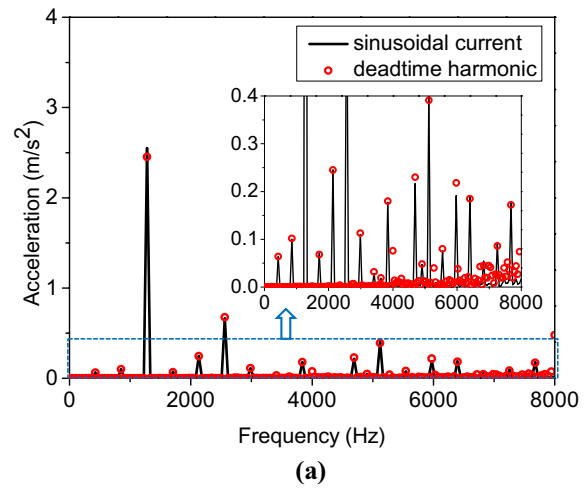


Fig. 19 Comparison of vibration and noise under sinusoidal and dead-time currents **a** vibration; **b** noise

force amplitudes. Here, the maximum peaks of vibration and noise at 1280 Hz are taken as examples to illustrate the specific impact of dead-time current harmonics. As shown in Fig. 19, both the vibration and noise peaks at 1280 Hz show a decrease when considering the dead-time current harmonics. Specifically, the vibration peak decrease from 2.55 to 2.45 m/s², while the noise peak decrease from 72.7 to 72.08 dB (A). Changes in vibration and noise peaks at 1280 Hz are closely related to the variation of the corresponding radial force, shown in Fig. 9. As the maximum peaks of vibration and noise mainly come from the 1280 Hz 0-order and 24-order radial forces, namely $f_r(0th, 1280\text{ Hz})$ and $f_r(24th, 1280\text{ Hz})$, so the specific contribution of dead-time current harmonics to these two force harmonics is theoretically derived according to (8).

First, the source of $f_r(0th, 1280\text{ Hz})$ is analyzed. According to (8) or Table 2, it can be deduced that the 0-order radial

force mainly comes from three parts: (1) interaction between the PM field and the permeance harmonic; (2) interaction between the PM field and the armature reaction field; (3) interaction of the PM field, the armature reaction field and the permeance harmonic. Thus, the following conditions should be met to generate 1280 Hz 0-order force

$$\begin{cases} (n_1 \pm n_2)p \pm uQ = 0 \\ (n_1 \pm n_2)pf = 1280 \end{cases} \text{ or } \begin{cases} (np \pm vN_r) \pm uQ = 0 \\ (n \pm s_{vh})pf = 1280 \end{cases} \quad (11)$$

here, when $u = 0$, the right part of (11) represents the interaction of PM field and armature reaction field, namely the third item of Table 2. Parameters such as the amplitude and phase sequence of current harmonics for this 8p24s ISPM SM are summarized in Table 5. By solving the left part of (11), the 1280 Hz 0-order force generated by the interaction of PM field and permeance harmonic can be deduced as

$$f_{r0}(0\text{th}, 1280 \text{ Hz}) = \frac{1}{4\mu_0} \lambda_0 \lambda_{a1} \times \left[B_{m1}B_{m5} + B_{m3}B_{m3} + \sum_{n=1,3,5,\dots} B_{mn}B_{m(n+6)} \right] \times \cos 24\omega t \quad (12)$$

Similarly, by solving the right part of (11), the contribution of current harmonics to 1280 Hz 0-order force can also be obtained.

The contribution of fundamental current can be calculated from

$$f_{r1}(0\text{th}, 1280 \text{ Hz}) = \frac{1}{2\mu_0} \lambda_0 \times \left\{ \begin{aligned} & B_{m5} \sum_{u=0}^{\infty} \lambda_{au} B_{a(5+6u)}^1 \\ & + B_{m7} \times \left[\lambda_{a1} B_{a1}^1 + \sum_{u=0}^{\infty} \lambda_{au} B_{a(7+6u)}^1 \right] \end{aligned} \right\} \times \sin(24\omega t + \theta_1) \quad (13)$$

The contribution of the 5th current harmonic can be calculated from

$$f_{r5}(0\text{th}, 1280 \text{ Hz}) = \frac{1}{2\mu_0} \lambda_0 \times \left\{ \begin{aligned} & B_{m1} \sum_{u=0}^{\infty} \lambda_{au} B_{a(1+6u)}^5 \\ & + B_{m11} \times \left[\lambda_{a1} B_{a1}^5 + \sum_{u=0}^{\infty} \lambda_{au} B_{a(11+6u)}^5 \right] \end{aligned} \right\} \times \sin(24\omega t + \theta_5) \quad (14)$$

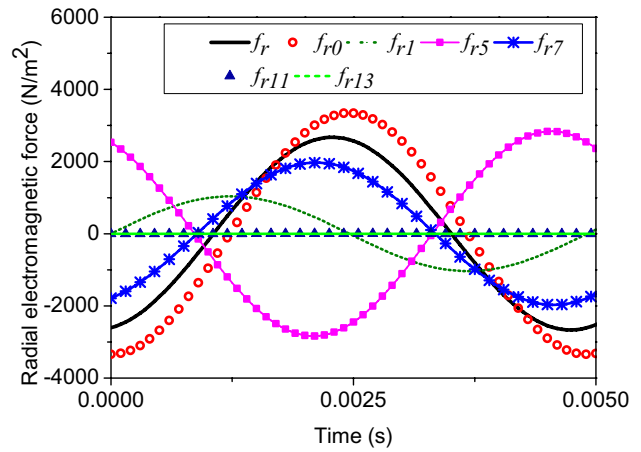


Fig. 20 Contribution of each source to 1280 Hz 0-order force

The contribution of the 7th current harmonic can be calculated from

$$f_{r7}(\text{0th}, 1280 \text{ Hz}) = \frac{1}{2\mu_0} \lambda_0 \times \left\{ \begin{array}{l} B_{m1} \sum_{u=0}^{\infty} \lambda_{au} B_{a(1+6u)}^7 \\ + B_{m13} \times \left[\lambda_{a1} B_{a7}^7 + \lambda_{a2} B_{a1}^7 + \sum_{u=0}^{\infty} \lambda_{au} B_{a(13+6u)}^7 \right] \end{array} \right\} \times \sin(24\omega t + \theta_7) \quad (15)$$

The contribution of the 11th current harmonic can be calculated from

$$f_{r11}(\text{0th}, 1280 \text{ Hz}) = \frac{1}{2\mu_0} \lambda_0 \times \left\{ \begin{array}{l} B_{m5} \sum_{u=0}^{\infty} \lambda_{au} B_{a(5+6u)}^{11} \\ + B_{m17} \times \left[\lambda_{a1} B_{a11}^{11} + \lambda_{a2} B_{a5}^{11} + \sum_{u=0}^{\infty} \lambda_{au} B_{a(17+6u)}^{11} \right] \end{array} \right\} \times \sin(24\omega t + \theta_{11}) \quad (16)$$

The contribution of the 13th current harmonic can be calculated from

$$f_{r13}(\text{0th}, 1280 \text{ Hz}) = \frac{1}{2\mu_0} \lambda_0 \times \left\{ \begin{array}{l} B_{m7} \times \left[\lambda_{a1} B_{a1}^{13} + \sum_{u=0}^{\infty} \lambda_{au} B_{a(7+6u)}^{13} \right] \\ + B_{m19} \times \left[\sum_{u=1}^3 \lambda_{au} B_{a(19-6u)}^{13} + \sum_{u=0}^{\infty} \lambda_{au} B_{a(19+6u)}^{13} \right] \end{array} \right\} \times \sin(24\omega t + \theta_{13}) \quad (17)$$

Thus, the total 1280 Hz 0-order force can be given as

$$f_r = f_{r0} + f_{r1} + f_{r5} + f_{r7} + f_{r11} + f_{r13}. \quad (18)$$

B_{mn} , B_{av}^h , and λ_{au} in (12)–(17) can be obtained analytically or numerically. Then, the contribution of each source can be calculated analytically, and the results are shown in Fig. 20. It can be seen that the total f_r mainly depends on f_{r0} , f_{r5} and f_{r7} . Due to specific phase relationships, the 7th current harmonic has a remarkable contribution to the total 1280 Hz 0-order force, while the 5th current harmonic has a weakening effect. Moreover, the weakening effect is dominant due to the large amplitude of the 5th current harmonic. Therefore, compared with the sinusoidal current condition, the amplitude of 1280 Hz 0-order force has a certain decrease

when considering dead-time current harmonics. This is consistent with the variation trend of $f_r(\text{0th}, 1280\text{Hz})$ in Fig. 9.

Similarly, the source of $f_r(24\text{th}, 1280 \text{ Hz})$ is also discussed. According to (8) or Table 2, the 24-order electromagnetic force mainly originates from the following three parts: (1) interaction of PM field harmonics; (2) interaction between the PM field and the armature reaction field; (3) interaction of the PM field, the armature reaction field and the permeance harmonic. Thus, the following conditions should be met to generate the 1280 Hz 24-order force

$$\begin{cases} (n_1 \pm n_2)p = 24 \\ (n_1 \pm n_2)pf = 1280 \end{cases} \text{ or } \begin{cases} (np \pm vN_t) \pm uQ = 24 \\ (n \pm s_{vh}h)pf = 1280 \end{cases} \quad (19)$$

By solving the left part of (19), the 1280 Hz 24-order force generated by the interaction of PM field harmonics can be deduced as

$$f_{r0}(24\text{th}, 1280 \text{ Hz}) = \frac{1}{4\mu_0} \lambda_0^2 \times \left[B_{m1}B_{m5} + B_{m3}B_{m3} + \sum_{n=1,3,5\dots} B_{mn}B_{m(n+6)} \right] \times \cos 24\omega t. \quad (20)$$

By solving the right part of (19), the contribution of fundamental current can be calculated from

$$f_{r1}(24\text{th}, 1280 \text{ Hz}) = \frac{1}{2\mu_0} \lambda_0 \times \left\{ \begin{array}{l} B_{m5} \times \left[\lambda_{a1} B_{a5}^1 + \sum_{u=0}^{\infty} \lambda_{au} B_{a(11+6u)}^1 \right] \\ + B_{m7} \times \left[\lambda_{a1} B_{a7}^1 + \lambda_{a2} B_{a1}^1 + \sum_{u=0}^{\infty} \lambda_{au} B_{a(13+6u)}^1 \right] \end{array} \right\} \times \sin(24\omega t + \theta_1). \quad (21)$$

The contribution of the 5th current harmonic can be calculated from

$$f_{r5}(24\text{th}, 1280 \text{ Hz}) = \frac{1}{2\mu_0} \lambda_0 \times \left\{ \begin{array}{l} B_{m1} \times \left[\lambda_{a1} B_{a1}^5 + \sum_{u=0}^{\infty} \lambda_{au} B_{a(7+6u)}^5 \right] \\ + B_{m11} \times \left[\lambda_{a1} B_{a11}^5 + \lambda_{a2} B_{a5}^5 + \sum_{u=0}^{\infty} \lambda_{au} B_{a(17+6u)}^5 \right] \end{array} \right\} \times \sin(24\omega t + \theta_5). \quad (22)$$

The contribution of the 7th current harmonic can be calculated from

$$f_{r7}(24\text{th}, 1280 \text{ Hz}) = \frac{1}{2\mu_0} \lambda_0 \times \left\{ \begin{array}{l} B_{m1} \times \left[\lambda_{a1} B_{a1}^7 + \sum_{u=0}^{\infty} \lambda_{au} B_{a(7+6u)}^7 \right] \\ + B_{m13} \times \left[\sum_{u=1}^3 \lambda_{au} B_{a(19-6u)}^7 + \sum_{u=0}^{\infty} \lambda_{au} B_{a(19+6u)}^7 \right] \end{array} \right\} \times \sin(24\omega t + \theta_7). \quad (23)$$

The contribution of the 11th current harmonic can be calculated from

$$f_{r11}(24\text{th}, 1280 \text{ Hz}) = \frac{1}{2\mu_0} \lambda_0 \times \left\{ \begin{array}{l} B_{m5} \times \left[\lambda_{a1} B_{a5}^{11} + \sum_{u=0}^{\infty} \lambda_{au} B_{a(11+6u)}^{11} \right] \\ + B_{m17} \times \left[\sum_{u=1}^3 \lambda_{au} B_{a(23-6u)}^{11} + \sum_{u=0}^{\infty} \lambda_{au} B_{a(23+6u)}^{11} \right] \end{array} \right\} \times \sin(24\omega t + \theta_{11}). \quad (24)$$

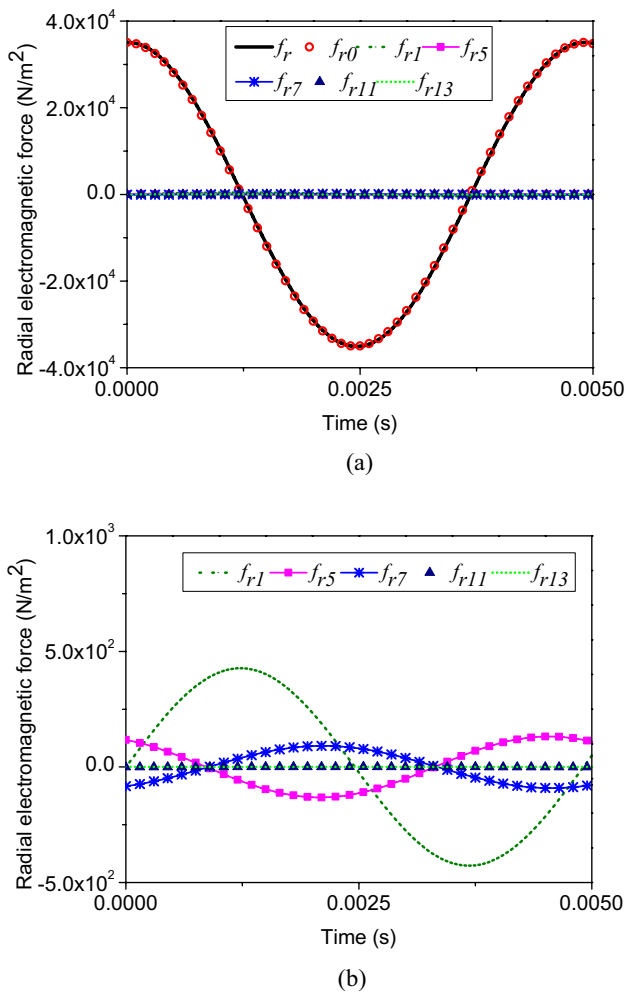


Fig. 21 Contribution of each source to 1280 Hz 24-order force **a** general drawing; **b** enlarged drawing

The contribution of the 13th current harmonic can be calculated from

$$f_{r13}(24\text{th}, 1280 \text{ Hz}) = \frac{1}{2\mu_0} \lambda_0 \times \left\{ \begin{aligned} &B_{m7} \times \left[\lambda_{a1} B_{a7}^{13} + \lambda_{a2} B_{a1}^{13} + \sum_{u=0}^{\infty} \lambda_{au} B_{a(13+6u)}^{13} \right] \\ &+ B_{m19} \times \left[\sum_{u=1}^4 \lambda_{au} B_{a(25-6u)}^{13} + \sum_{u=0}^{\infty} \lambda_{au} B_{a(25+6u)}^{13} \right] \end{aligned} \right\} \times \sin(24\omega t + \theta_{13}). \tag{25}$$

Thus, the total 1280 Hz 24-order force can be written as

$$f_r = f_{r0} + f_{r1} + f_{r5} + f_{r7} + f_{r11} + f_{r13}. \tag{26}$$

The contribution of each source to f_r (24th, 1280Hz) is also obtained analytically, and the results are shown in Fig. 21. For PM motors, the PM field is dominant in the air gap. As a result, the interaction of PM field harmonics has a dominant contribution to the total 1280 Hz 24-order force, as shown in Fig. 21a. Moreover, as shown in Fig. 21b, the fundamental current and the 7th current harmonic have certain contributions to the total 1280 Hz 24-order force, while the 5th current harmonic has a weakening effect. Hence, compared with the sinusoidal current condition, the amplitude of 1280 Hz 24-order force has a slight decrease due to the existence of the 5th current harmonic. This is also consistent with the variation trend of the 1280 Hz 24-order force in Fig. 9.

Since the amplitudes of 1280 Hz 0-order and 24-order force have a certain decrease, the vibration and noise peaks at 1280 Hz also have a slight decline when considering dead-time current harmonics. Thus, the variation of the maximum vibration and noise peaks is well explained. Similar theoretical analysis can also be performed to illustrate the variation trend of vibration and noise peaks at other frequencies, which has a significant guidance for the reduction of electromagnetic vibration and noise.

Conclusion

Considering the dead-time current harmonics, the radial electromagnetic force and vibroacoustic behavior of ISPMSMs were studied in detail in this paper. The spatio-temporal characteristics of radial force were analytically derived. Then, the vibration and noise of an 8p24s ISPMSM used for EVs were predicted by a multiphysics model considering the structural orthotropy of the stator and the non-uniform distribution of the radial force. Moreover, the vibroacoustic mechanism of the ISPMSM was revealed and

the specific influence of dead-time current harmonics on vibration and noise was analyzed. The main conclusions are summarized as follows.

1. The spatial orders of the radial force in ISPMSMs contain 0 and 2 kp, while the frequency is 2 kpf. The intro-

duction of $(6k \pm 1)$ th dead-time current harmonics will not induce extra spatial orders and frequency components of radial force, but will change the amplitude.

2. Different from fractional-slot motors, the 0-order and 2-order modal responses commonly caused by the 0-order and slot-order radial force are the roots of vibration and noise in ISPMsMs. The former satisfies the spatial match with the corresponding radial force, while the latter satisfies the frequency match. Since the frequency of both the 0-order and slot-order radial force is 6 kpf, the main peaks of vibration and noise of the ISPMsM appear at 6 kpf.
3. The dead-time current harmonics have a significant impact on vibration and noise peaks by changing the amplitudes of corresponding radial force harmonics. Moreover, the specific influence of dead-time current harmonics depends on their amplitudes and phase angles.

This study provides guidance for the accurate calculation and analysis of electromagnetic vibration and noise, which is beneficial for the design of low-vibration and noise ISPMsMs.

Acknowledgements This work was supported by a Grant (Project 51875410) from the National Natural Science Foundation of China.

Declarations

Conflict of Interest The authors declare that they have no known competing financial interests or personal relationships that could have appeared to influence the work reported in this paper.

References

1. Zhang Z, Dong Y, Han Y (2020) Dynamic and control of electric vehicle in regenerative braking for driving safety and energy conservation. *J Vib Eng Technol* 8:179–197. <https://doi.org/10.1007/s42417-019-00098-0>
2. Wei Y, Si J, Cheng Z (2020) Design and characteristic analysis of a six-phase direct-drive permanent magnet synchronous motor with 60 degrees phase-belt toroidal winding configuration for electric vehicle. *IET Electr Power Appl* 14:2659–2666
3. He C, Li S, Shao K et al (2021) Robust iterative feedback tuning control of a permanent magnet synchronous motor with repetitive constraints: a Udwadia–Kalaba approach. *J Vib Eng Technol*. <https://doi.org/10.1007/s42417-021-00365-z>
4. Liu X, Chen H, Zhao J et al (2016) Research on the performances and parameters of interior PMSM used for electric vehicles. *IEEE Trans Ind Electron* 63:3533–3545
5. Ma C, Chen C, Liu Q (2017) Sound quality evaluation of the interior noise of pure electric vehicle based on neural network model. *IEEE Trans Ind Electron* 64:9442–9450
6. Ma C, Li Q, Liu Q, Wang D (2016) Sound quality evaluation of noise of hub permanent-magnet synchronous motors for electric vehicles. *IEEE Trans Ind Electron* 63:5663–5673
7. Li S, Su Y, Shen C (2018) Noise analysis and control on motor starting and accelerating of electric bus. *J Vib Eng Technol* 6:93–99. <https://doi.org/10.1007/s42417-018-0019-2>
8. Wu S, Zuo S, Wu X et al (2017) Vibroacoustic prediction and mechanism analysis of claw pole alternators. *J IEEE Trans Ind Electron* 64:4463–4473
9. Jang I et al (2014) Method for analyzing vibrations due to electromagnetic force in electric motors. *IEEE Trans Magn* 50:297–300
10. Islam R, Husain I (2010) Analytical model for predicting noise and vibration in permanent-magnet synchronous motors. *IEEE Trans Ind Appl* 46:2346–2354
11. Hu S, Zuo S, Wu H et al (2019) An analytical method for calculating the natural frequencies of a motor considering orthotropic material parameters. *IEEE Trans Ind Electron* 66:7520–7528
12. Deng W, Zuo S (2018) Analytical modeling of the electromagnetic vibration and noise for an external-rotor axial-flux in-wheel motor. *IEEE Trans Ind Electron* 65:1991–2000
13. Wang X, Sun X, Gao P (2019) A study on the effects of rotor step skewing on the vibration and noise of a PMSM for electric vehicles. *IET Electr Power Appl* 14(1):131
14. Wang S, Hong J, Sun Y, Cao H (2020) Effect comparison of zig-zag skew pm pole and straight skew slot for vibration mitigation of PM brush DC motors. *IEEE Trans Ind Electron* 67:4752–4761
15. Kim DY, Jang GH, Nam JK (2013) Magnetically induced vibrations in an IPM motor due to distorted magnetic forces arising from flux weakening control. *IEEE Trans Magn* 49:3929–3932
16. Zuo S, Lin F, Wu X (2015) Noise analysis, calculation, and reduction of external rotor permanent-magnet synchronous motor. *IEEE Trans Ind Electron* 62:6204–6212
17. Dong Q, Liu X, Qi H (2020) Vibro-acoustic prediction and evaluation of permanent magnet synchronous motors. *Proc Inst Mech Eng Part D J Automot Eng* 234:2783–2793
18. Lin F, Zuo S, Deng W et al (2018) Modeling and analysis of acoustic noise in external rotor in-wheel motor considering Doppler effect. *IEEE Trans Ind Electron* 65:4524–4533
19. Deng W, Zuo S (2018) Axial force and vibroacoustic analysis of external-rotor axial-flux motors. *IEEE Trans Ind Electron* 65:2018–2030
20. Dorneles-Callegaro A, Liang J, Jiang JW, Bilgin B, Emadi A (2019) Radial force density analysis of switched reluctance machines: the source of acoustic noise. *IEEE Trans Transport Electrif.* 5:93–106
21. Mcdevitt TE, Campbell RL, Jenkins DM (2004) An investigation of induction motor zeroth-order magnetic stresses, vibration, and sound radiation. *IEEE Trans Magn* 40:774–777
22. Besnerais JL, Lanfranchi V, Hecquet M et al (2010) Characterization and reduction of audible magnetic noise due to PWM supply in induction machines. *IEEE Trans Ind Electron* 57:1288–1295
23. Valavi M, Besnerais JL, Nysveen A (2016) An investigation of zeroth-order radial magnetic forces in low-speed surface-mounted permanent magnet machines. *IEEE Trans Magn* 52:1–6

24. Fang H, Li D, Qu R et al (2019) Modulation effect of slotted structure on vibration response in electrical machines. *IEEE Trans Ind Electron* 66:2998–3007
25. Wang S, Hong J, Sun Y et al (2019) Analysis of zeroth mode slot frequency vibration of integer slot permanent magnet synchronous motors. *IEEE Trans Ind Electron* 67:2954–2964
26. Liang W, Wang J, Luk CK et al (2014) Analytical modeling of current harmonic components in PMSM drive with voltage-source inverter by SVPWM technique. *IEEE Trans Energy Convers* 29:673–680
27. Liang W, Fei W, Luk CK (2016) An improved sideband current harmonic model of interior PMSM drive by considering magnetic saturation and cross-coupling effects. *IEEE Trans Ind Electron* 63:4097–4104
28. Tsoumas IP, Tischmacher H (2014) Influence of the inverter's modulation technique on the audible noise of electric motors. *IEEE Trans Ind Appl* 50:269–278
29. Andersson A, Lennström D, Nykänen A (2016) Influence of inverter modulation strategy on electric drive efficiency and perceived sound quality. *IEEE Trans Transport Electrif* 2:24–35
30. Deng W, Zuo S (2019) Comparative study of sideband electromagnetic force in internal and external rotor PMSMs with SVPWM technique. *IEEE Trans Ind Electron* 66:956–966

Publisher's Note Springer Nature remains neutral with regard to jurisdictional claims in published maps and institutional affiliations.